

Dynamics of Coronavirus Replication-Transcription Complexes^{∇†}

Marne C. Hagemeijer,^{1‡} Monique H. Verheije,^{1‡§} Mustafa Ulasli,² Indra A. Shaltiël,¹
Lisa A. de Vries,¹ Fulvio Reggiori,² Peter J. M. Rottier,¹ and Cornelis A. M. de Haan^{1*}

Virology Division, Department of Infectious Diseases and Immunology, Faculty of Veterinary Medicine, Utrecht University, Utrecht, The Netherlands,¹ and Department of Cell Biology and Institute of Biomembranes, University Medical Centre Utrecht, Utrecht, The Netherlands²

Received 15 August 2009/Accepted 24 November 2009

Coronaviruses induce in infected cells the formation of double-membrane vesicles (DMVs) in which the replication-transcription complexes (RTCs) are anchored. To study the dynamics of these coronavirus replicative structures, we generated recombinant murine hepatitis coronaviruses that express tagged versions of the nonstructural protein nsp2. We demonstrated by using immunofluorescence assays and electron microscopy that this protein is recruited to the DMV-anchored RTCs, for which its C terminus is essential. Live-cell imaging of infected cells demonstrated that small nsp2-positive structures move through the cytoplasm in a microtubule-dependent manner. In contrast, large fluorescent structures are rather immobile. Microtubule-mediated transport of DMVs, however, is not required for efficient replication. Biochemical analyses indicated that the nsp2 protein is associated with the cytoplasmic side of the DMVs. Yet, no recovery of fluorescence was observed when (part of) the nsp2-positive foci were bleached. This result was confirmed by the observation that preexisting RTCs did not exchange fluorescence after fusion of cells expressing either a green or a red fluorescent nsp2. Apparently, nsp2, once recruited to the RTCs, is not exchanged with nsp2 present in the cytoplasm or at other DMVs. Our data show a remarkable resemblance to results obtained recently by others with hepatitis C virus. The observations point to intriguing and as yet unrecognized similarities between the RTC dynamics of different plus-strand RNA viruses.

Viruses have evolved elaborate strategies to manipulate and exploit host cellular components and pathways to facilitate various steps of their replication cycle. One common feature among plus-strand RNA viruses is the assembly of their replication-transcription complexes (RTCs) in association with cytoplasmic membranes (reviewed in references 41, 44, and 54). The induction and modification of replicative vesicles seem to be beneficial to the virus (i) in orchestrating the recruitment of all cellular and viral constituents required for viral RNA synthesis and (ii) in providing a protective microenvironment against virus-elicited host defensive (immune) mechanisms.

The enveloped coronaviruses (CoVs) possess impressively large plus-strand RNA genomes, with sizes ranging from ~27 to 32 kb (22). The coronavirus polycistronic genome can roughly be divided into two regions: the first two-thirds of the genome contains the large replicase gene that encodes the proteins collectively responsible for viral RNA replication and transcription while the remaining 3'-terminal part of the genome encodes the structural proteins and some accessory proteins that are expressed from a nested set of subgenomic mRNAs (sgmRNAs) (55).

Almost all of the constituents of the coronavirus RTCs are encoded by the large replicase gene that is comprised of two partly overlapping open reading frames (ORFs), ORF1a and ORF1b. Translation of these ORFs results in two very large polyproteins, pp1a and pp1ab, the latter of which is produced by translational readthrough via a -1 ribosomal frameshift induced by a “slippery” sequence and a pseudoknot structure at the end of ORF1a (46, 69). pp1a and pp1ab are extensively processed into an elaborate set of nonstructural proteins (nsps) via co- and posttranslational cleavages by the viral papain-like proteinase(s) (PLpro) residing in nsp3 and the 3C-like main proteinase (Mpro) in nsp5 (17, 51, 64, 66, 77). The functional domains present in the replicase polyproteins are conserved among all coronaviruses (77). The ORF1a-encoded nsps (nsp1 to nsp11) contain, among others, the viral proteinases (17, 51, 64, 66, 77), the membrane-anchoring domains (34, 48, 49), anti-host immune activities (8, 32, 47, 78), and predicted and identified RNA-binding and RNA-modifying activities (20, 27, 31, 43, 67, 76). ORF1b (nsp12 to nsp16) encodes the key enzymes directly involved in RNA replication and transcription, such as the RNA-dependent RNA polymerase (RdRp) and the helicase (2, 7, 11, 18, 29, 30, 33, 45, 60). The nsps collectively form the RTCs; however, the size and complexity of these complexes are unknown.

Coronavirus replicative structures consist of double-membrane vesicles (DMVs) in which the RTCs are anchored (3, 23, 65). Although hardly anything is known about the mechanism by which the DMVs are induced, recent studies by us and others indicate that the DMVs are most likely derived from the endoplasmic reticulum (ER). Electron microscopy (EM) analyses of infected cells showed the partial colocalization of nsps with an ER protein marker while the DMVs were often found

* Corresponding author. Mailing address: Virology Division, Department of Infectious Diseases and Immunology, Utrecht University, Yalelaan 1, 3584 CL Utrecht, The Netherlands. Phone: 31 30 253 4195. Fax: 31 30 253 6723. E-mail: C.A.M.deHaan@uu.nl.

§ Present address: Pathology Division, Department of Pathobiology, Faculty of Veterinary Medicine, Utrecht University, Utrecht, The Netherlands.

‡ M.C.H. and M.H.V. contributed equally to the manuscript.

† Supplemental material for this article may be found at <http://jvi.asm.org/>.

∇ Published ahead of print on 9 December 2009.

in close proximity to the ER and, occasionally, in continuous association with it (35, 65). More recently, the DMVs were reported to be integrated into a reticulovesicular network of modified ER membranes, also referred to as convoluted membranes (CMs) (35). In addition, when expressed in the absence of a coronavirus infection, nsp3, nsp4, and nsp6 were inserted into the ER (26, 34, 48, 49). When expressed in coronavirus-infected cells, nsp4 appeared to exit the ER and to be recruited to the RTCs (49). Furthermore, coronavirus replication was severely affected when the formation of COPI- and COPII-coated vesicles in the early secretory pathway was inhibited by the addition of drugs, by the expression of dominant negative mutants, or by depletion of host proteins using RNA interference (49, 72).

The mechanisms underlying the assembly of membrane-associated replication complexes in cells infected with plus-strand RNA viruses are just beginning to be unraveled. Previous studies have provided valuable information on the formation of the virus-induced replicative structures, resulting, however, in a static view of these processes inherent to the cell biological techniques used. Thus, insight into the dynamics of these structures is largely lacking, certainly in the case of coronaviruses. In the present study, we made the first step to fill this gap by performing live-cell imaging analyses of mouse hepatitis coronavirus (MHV) replicative structures in combination with fluorescent recovery after photobleaching (FRAP) studies. This approach allowed us to monitor the coronavirus DMV-anchored RTCs in real time and generated new insights into the dynamics of these virus-induced structures, revealing striking similarities between the replicative structures induced by MHV and those generated by the unrelated hepatitis C virus (HCV).

MATERIALS AND METHODS

Cells, viruses, and antibodies. HeLa-CEACAM1a (75), *Felis catus* whole fetus (FCWF) cells (American Type Culture Collection) and murine LR7 fibroblast cells (36) were maintained as monolayer cultures in Dulbecco's modified Eagle's medium (DMEM^{-/-}; Cambrex BioScience) containing 10% fetal calf serum (FCS; Bodinco BV), 100 IU/ml of penicillin, and 100 µg/ml of streptomycin (both from Life Technologies; this medium is referred to as DMEM^{+/+}).

MHV strain A59, recombinant wild-type MHV (MHV-WT) (13), recombinant MHV-ERLM (12), which expresses the *Renilla* luciferase (RL) gene, and the recombinant viruses generated in this study, MHV-nsp2GFP (where GFP is green fluorescent protein), MHV-nsp2mCherry, and MHV-nsp2RL, were propagated in LR7 cells.

Antibody directed against double-stranded RNA (dsRNA) (K1) or the GFP was purchased from English and Scientific Consulting Bt. (58) and Immunology Consultants Laboratory, Inc., respectively. The polyclonal anti-p22 antibody, which is directed against MHV nsp8 (39), the monoclonal M_N antibody, recognizing the N-terminal domain of the MHV membrane (M) protein (68), and the polyclonal anti-D3 (nsp2/nsp3) and anti-D11 (nsp4) rabbit antibodies (9) were kindly provided by Mark Denison, John Flemming, and Susan Baker, respectively. The peptide serum recognizing the C-terminal tail (anti-M_C) of the MHV M protein has been described before (38).

Plasmids. The MHV A59 nsp2 gene fragment was generated by reverse transcriptase (RT)-PCR amplification of viral genomic RNA using the primers indicated in Table 1. The obtained PCR product was cloned into the pGEM-T Easy vector (Promega), which resulted in the pGEM-nsp2 plasmid. This plasmid was used as the starting point for the generation of the other nsp2-encoding plasmids that were subsequently used for the generation of recombinant viruses and for expression studies. Gene fragments, encoding C- and/or N-terminal nsp2 deletion mutants, were generated by PCR using the primers indicated in Table 1 and cloned into the pGEM-T Easy vector, generating pGEM-nsp2AB (nsp2 residues 1 to 247), pGEM-nsp2BC (nsp2 residues 122 to 459), and pGEM-nsp2CD (nsp2 residues 247 to 585). The nsp2-encoding gene fragments were subsequently

TABLE 1. Primers used in this study

Primer no.	Polarity	Sequence (5'→3')	Position in the viral genome (nt) ^a
3327	+	GAATTCGATATCATGGTTAAGCC GATCCTGTTTG	951
3328	-	AGATCTCGCACAGGGAAACCT CCAG	2705
3524	+	GATATCATGGAATTCTGTTATAA AACCAAGC	1314
3525	-	AGATCTACCAACTACTCTGTGA TAAG	1691
3527	+	GATATCATGGGTTGTAAGGCAAT TGTTT	1689
3528	-	AGATCTAACCTGAAAAATGC CTTG	2328

^a nt, nucleotide.

cloned into the pEGFP-N3 vector (Clontech), resulting in pEGFP-nsp2 (where EGFP is enhanced GFP), pEGFP-nsp2AB, pEGFP-nsp2BC, and pEGFP-nsp2CD (Fig. 1B).

Three RNA transcription vectors (pMH54-nsp2EGFP, pMH54-nsp2mCherry, and pMH54-nsp2RL) were generated in order to create recombinant MHVs expressing the gene encoding nsp2 tagged with either EGFP (Clontech), mCherry (Clontech), or *Renilla* luciferase (Invitrogen) at the genomic position of the hemagglutinin esterase (HE) gene. These vectors were constructed similarly as described previously for pMH54-nsp4EGFP (49), with the exception that the nsp2 rather than the nsp4 gene fragment was cloned in frame with either EGFP-, mCherry-, or RL-encoding sequences.

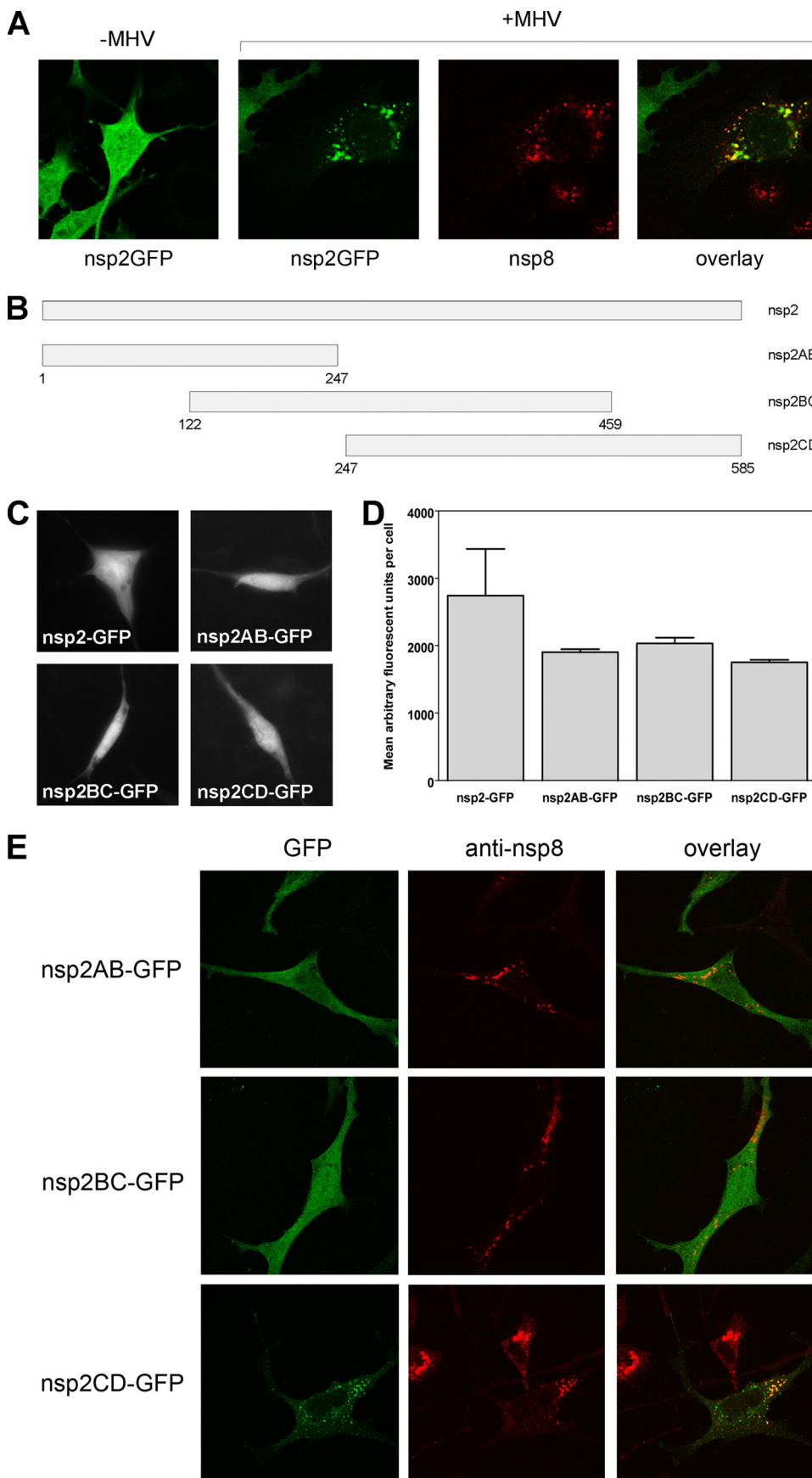
The expression plasmid encoding alpha-tubulin as a yellow fluorescent protein (YFP) fusion construct (pYFP-alpha-tubulin) was obtained from Euroscarf (1). The pER-GFP construct encoding an ER-retained GFP protein was kindly provided by Frank van Kuppeveld. The GFP coding region in this plasmid was replaced by that of firefly luciferase (Fluc) using conventional cloning techniques, resulting in pER-Fluc. All constructs were confirmed by restriction and/or sequence analysis.

Targeted recombination. Incorporation of the nsp2 expression cassettes into the MHV genome by targeted RNA recombination, resulting in recombinant MHV-nsp2GFP, MHV-nsp2mCherry, and MHV-nsp2RL viruses, was carried out as previously described (36). Briefly, donor RNA transcribed from the linearized transcription vectors was electroporated into FCWF cells that had been infected earlier with the interspecies chimeric coronavirus fMHV (an MHV derivative in which the spike ectodomain is of feline coronavirus origin) (36). These cells were plated onto a monolayer of murine LR7 cells. After 24 h of incubation at 37°C, progeny viruses released into the culture medium were harvested and plaque purified twice on LR7 cells before a passage 1 stock was grown. After confirmation of the recombinant genotypes, passage 2 stocks were grown that were subsequently used in the experiments.

Infection and transfection. Subconfluent monolayers of LR7 cells were transfected by overlaying the cells with a mixture of 0.5 ml of OptiMem (Invitrogen), 1 µl of Lipofectamine 2000 (Invitrogen), and 1 µg of each selected construct, followed by incubation at 37°C. Three hours after transfection, the medium was replaced by DMEM^{+/+}. Where indicated, 24 h after transfection the cells were inoculated with (recombinant) MHV A59 at a multiplicity of infection (MOI) of 1 to 10 for 1 h before the inoculum was replaced by fresh DMEM^{+/+}.

One-step growth curve(s). LR7 cells grown in 0.33-cm² tissue culture dishes were infected in parallel using an MOI of 10 for 1 h at 37°C in 5% CO₂. After adsorption, the cells were washed with phosphate-buffered saline (PBS) supplemented with 50 mM Ca²⁺ and 50 mM Mg²⁺ three times, and incubation was continued in DMEM^{+/+}. Viral infectivity in culture medium at different times postinfection (p.i.) was determined by a quantal assay on LR7 cells, and the 50% tissue culture infective dose (TCID₅₀) values were calculated.

Metabolic labeling and immunoprecipitation. Subconfluent monolayers of LR7 cells in 10-cm² tissue culture dishes were infected with the viruses indicated in Fig. 2F for 1 h at an MOI of 10, after which the inoculum was removed; the cells were then washed three times with DMEM^{+/+}, and incubation was continued in DMEM^{+/+}. At 5.5 h p.i., the cells were starved for 30 min in cysteine- and methionine-free modified Eagle's medium containing 10 mM HEPES (pH 7.2) and 5% dialyzed FCS. This medium was replaced with 1 ml of a similar



medium containing 100 μCi of ^{35}S *in vitro* cell labeling mixture (Amersham), after which the cells were further incubated for 3 h. The cells were washed once with PBS supplemented with 50 mM Ca^{2+} and 50 mM Mg^{2+} and then lysed on ice in 1 ml of lysis buffer (0.5 mM Tris [pH 7.3], 1 mM EDTA, 0.1 M NaCl, 1% Triton X-100). The lysates were cleared by centrifugation for 5 min at 15,000 rpm and 4°C and used in radioimmunoprecipitation studies. Aliquots of the cell lysates were diluted in 1 ml of detergent buffer (50 mM Tris [pH 8.0], 62.5 mM EDTA, 1% NP-40, 0.4% sodium deoxycholate, 0.1% SDS) containing antibodies (4 μl of rabbit anti-nsp2/nsp3). After overnight incubation at 4°C , the immune complexes were adsorbed to Pansorbin cells (Calbiochem) for 60 min at 4°C and subsequently collected by centrifugation. The pellets were washed three times by resuspension and centrifugation with radioimmunoprecipitation assay (RIPA) buffer (10 mM Tris [pH 7.4], 150 mM NaCl, 0.1% SDS, 1% NP-40, 1% sodium deoxycholate). The final pellets were suspended in Laemmli sample buffer (LSB) and heated at 95°C for 1 min before analysis by SDS-polyacrylamide gel electrophoresis (PAGE) with 12.5% polyacrylamide gels. The radioactivity in protein bands was quantitated in dried gels using a PhosphorImager (Molecular Dynamics).

Quantitative RT-PCR. Total RNA was isolated from infected cells using TRIzol reagent (Invitrogen), after which it was purified using an RNeasy minikit (Qiagen), both according to the manufacturer's instructions. Relative gene expression levels of viral (sub)genomic RNA was determined by performing quantitative RT-PCR using Assay-On-Demand reagents (PE Applied Biosystems) as described previously (14, 52). Reactions were performed using an ABI Prism 7000 sequence detection system. The comparative threshold cycle (C_T) method was used to determine the fold change for each individual gene.

Immunofluorescence confocal microscopy. LR7 cells grown on glass coverslips were fixed at the times indicated in the text and figure legends after transfection or infection using a 4% paraformaldehyde (PFA) solution in PBS for 30 min at room temperature. The fixed cells were washed with PBS and permeabilized using either 0.1% Triton X-100 for 10 min at room temperature or 0.5 $\mu\text{g}/\text{ml}$ digitonin (diluted in 0.3 M sucrose, 25 mM MgCl_2^{2+} , 0.1 M KCl, 1 mM EDTA, 10 mM PIPES [piperazine- N,N' -bis(2-ethanesulfonic acid)], pH 6.8) for 5 min at 4°C . Next, the permeabilized cells were washed with PBS and incubated for 15 min in blocking buffer (PBS–10% normal goat serum), followed by a 60-min incubation with antibodies directed against either nsp4, nsp8, MHV M, EGFP, or dsRNA. After three washes with PBS, the cells were incubated for 45 min with Cy3-conjugated donkey anti-rabbit immunoglobulin G antibodies (Jackson Laboratories), fluorescein isothiocyanate-conjugated goat anti-rabbit immunoglobulin G antibodies (ICN), or Cy3-conjugated donkey anti-mouse immunoglobulin G antibodies (Jackson Laboratories). Where indicated, nuclei of cells were stained with TOPRO 3 iodide (Molecular Probes). After four washes with PBS, the samples were mounted on glass slides in FluorSave (Calbiochem). The samples were examined with a confocal fluorescence microscope (Leica TCS SP), or fluorescence intensities were quantified using a DeltaVision RT microscope and software from Applied Precision, Inc. (API).

Time-lapse live-cell imaging and photobleaching. Subconfluent monolayers of LR7 cells were grown in 0.8-cm 2 Lab-Tek Chambered Coverglasses (Thermo Fisher Scientific and Nunc GmbH & Co. KG). The cells were transfected and infected as described above. Where indicated in the text and figure legends, cells were incubated with or without 1 μM nocodazole in DMEM $+/+$ at 4°C for 1 h, after which the cells were transferred to 37°C , and incubation was continued. Live-cell digital images of cells, placed in an environmental chamber at 37°C , were acquired at $\times 100$ magnification by the DeltaVision RT microscope from Applied Precision, Inc. (API). Images were deconvolved and analyzed using SoftWorx software (API). Time-lapse movies in QuickTime format were generated using ImageJ software, version 1.41(W. S. Rasband, NIH, Bethesda, MD [http://rsb.info.nih.gov/ij/]). Particle tracking was performed using the MTrackJ plug-in for ImageJ developed by Erik Meijering at the Biomedical Imaging Group Rotterdam (Erasmus Medical Centre, Rotterdam, The Netherlands).

FRAP experiments were performed using the quantifiable laser module

(QLM) of the DeltaVision RT microscope at 37°C . For each FRAP experiment, five prebleach images were collected, followed by a 1-s, 488-nm laser pulse with a radius of 0.500 μm to bleach the regions of interest (ROI). In a time frame of 60 s, 52 additional images were captured. Quantitative analysis of the FRAP data was performed using SoftWorx software.

Differential ultracentrifugation and protease protection assay. Subconfluent monolayers of LR7 cells were transfected and/or infected as described above and washed once with PBS before being scraped in homogenization buffer (HB; 50 mM Tris-HCl [pH 7.2] and 10 mM sucrose) and centrifuged for 5 min at 1,200 rpm. Cells were subsequently resuspended in HB, and homogenized cell lysates were prepared by repeated passage through a 21-gauge needle. The differential ultracentrifugation was performed in a Beckman Coulter Optima Max-E ultracentrifuge using a TLA-55 rotor. First, the homogenized cells were centrifuged for 10 min at 3,000 rpm to remove the nuclei and the cellular debris. The resulting supernatant was next centrifuged for 20 min at 23,000 rpm to separate the intracellular membranes (pellet) from the cytosol (supernatant). Where indicated in the text and figure legends, the intracellular membrane fractions were mock treated or treated with 20 $\mu\text{g}/\text{ml}$ proteinase K for 10 min at 20°C in the presence or absence of 0.05% TX-100 before proteinase K was inactivated by the addition of 2 mM phenylmethylsulfonyl fluoride (PMSF). *Renilla* and firefly luciferase activity in the different fractions was determined using a Dual-Luciferase Assay Kit (Promega) according to the manufacturer's instructions.

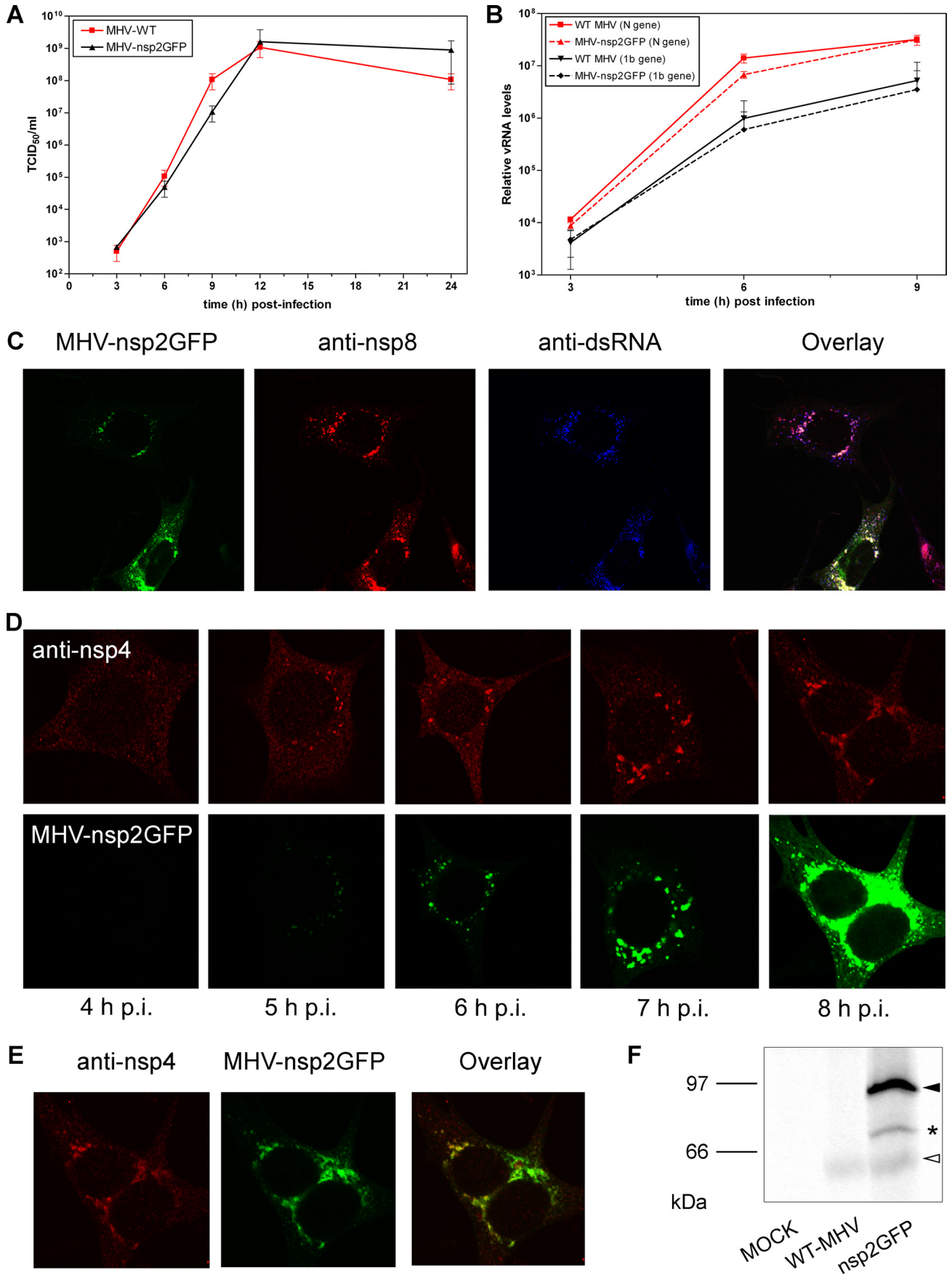
EM procedures. HeLa-CEACAM1a cells infected with recombinant MHV-nsp2GFP were processed for conventional EM and cryo-immuno-EM (IEM) at 8 h p.i. as previously described (63, 72). Cryo-sections were immunolabeled using a polyclonal anti-GFP (Abcam, Cambridge, United Kingdom) antibody, followed by incubation with protein A-gold conjugates prepared following an established protocol (63). Sections were viewed in a JEOL 1010 or a JEOL 1200 electron microscope (JEOL, Tokyo, Japan), and images were recorded on Kodak 4489 sheet films (Kodak, Rochester, NY).

RESULTS

MHV nsp2 is efficiently recruited to the RTCs. To enable live-cell imaging of coronavirus RTCs in infected cells, we needed to visualize these structures in living cells. Previously, we along with others have shown that (GFP-tagged) nsp2 is efficiently recruited to perinuclear foci in MHV-infected cells (24, 72). To confirm and extend these observations, GFP-tagged nsp2 (nsp2-GFP) was expressed in *trans* in mouse cells that were subsequently infected with MHV or mock infected. Next, the colocalization of nsp2-GFP with nsp8, an established marker for the RTCs (39), was monitored. In the absence of a MHV infection, nsp2-GFP demonstrated a diffuse cytosolic and nuclear fluorescence pattern (Fig. 1A). Upon infection with MHV, nsp2 appeared to be efficiently recruited to the RTCs as this protein was redistributed almost completely to punctuate perinuclear foci, colocalizing with nsp8 (Fig. 1A).

To investigate the recruitment of nsp2 to the RTCs in more detail, we investigated which part of the protein was responsible for this phenotype. To this end, we generated plasmids that encoded nsp2 truncations C-terminally fused with GFP (Fig. 1B). In the absence of a MHV infection, all proteins demonstrated a cytosolic and nuclear expression pattern (Fig. 1C). The different nsp2 truncation mutants displayed very similar

FIG. 1. Recruitment of MHV nsp2 to the RTCs. (A) LR7 cells transfected with pEGFP-nsp2 were mock infected ($-$ MHV) or infected with MHV A59 ($+$ MHV). Cells were fixed at 6 h p.i. and subsequently processed for immunofluorescence analysis using antibodies against nsp8. (B) Schematic representation of the C- and N-terminal truncations of MHV nsp2. The amino acids remaining are indicated. The EGFP tag at the C-terminal end of nsp2 is not indicated. (C and D) LR7 cells transfected with pEGFP-nsp2, pEGFP-nsp2AB, pEGFP-nsp2BC, or pEGFP-nsp2CD were fixed at 30 h posttransfection and processed for microscopic analysis (C); in addition, the mean arbitrary fluorescent intensities of 25 cells were determined using a DeltaVision RT microscope and software from Applied Precision (D). (E) LR7 cells transfected with pEGFP-nsp2AB, pEGFP-nsp2BC, or pEGFP-nsp2CD were mock infected or infected with MHV-A59. At 6 h p.i. the cells were fixed and processed for immunofluorescence analysis using nsp8 antibodies.



expression levels, which were only slightly lower than the level of the full-length nsp2-GFP fusion protein (Fig. 1D).

Next, these plasmids were used in the redistribution assay as described above. Cells expressing the nsp2AB and nsp2BC truncations exhibited a diffuse nuclear and cytoplasmic fluorescence, regardless of whether these cells were mock infected (Fig. 1C) or infected with MHV (Fig. 1E). No colocalization of these proteins with the nsp8 RTC marker protein was observed. In contrast, the nsp2CD truncation localized to perinuclear dots positive for nsp8 in infected cells. Based on these results, we concluded that the carboxy-terminal part of the nsp2 protein is required and sufficient to target the nsp2-GFP fusion proteins to the replication sites.

Recombinant MHVs expressing nsp2 fusion proteins. To facilitate the live-cell imaging of coronavirus RTCs during coronavirus infection, we next generated recombinant MHVs expressing nsp2 tagged either with GFP (MHV-nsp2GFP) or with a red fluorescent protein (MHV-nsp2mCherry). In these viruses, the gene encoding the nsp2 fusion protein was incorporated into the viral genome as an additional expression cassette, using a previously described targeted RNA recombination system (36). The nsp2-GFP or the nsp2-mCherry gene, each one preceded by a transcription-regulatory sequence, replaced the nonfunctional HE gene.

The generated recombinant viruses were evaluated for their growth kinetics and viral RNA synthesis. As a control, we used a recombinant wild-type MHV A59 (MHV-WT). MHV-nsp2GFP replicated efficiently in cell culture with titers that were only slightly lower than those of MHV-WT in a one-step growth curve (Fig. 2A). In agreement with these results, viral RNA synthesis, as determined by quantitative RT-PCR on the 1b and the N gene, was only slightly affected by the insertion of the nsp2-GFP expression cassette into the viral genome (Fig. 2B). MHV-nsp2mCherry replicated to the same extent as MHV-nsp2GFP (data not shown).

Next, we studied the subcellular localization of the nsp2 fusion proteins by immunofluorescence. Only the results for MHV-nsp2GFP are shown since essentially identical results were obtained for MHV-nsp2mCherry. As shown in Fig. 2C, cells infected with MHV-nsp2GFP revealed at 6 h p.i. a GFP fluorescence distribution pattern identical to the one observed when nsp2-GFP was expressed from a plasmid in MHV-infected cells (compare Fig. 1A and 2C). Importantly, nsp2-GFP localized to perinuclear foci positive not only for nsp8 but also for dsRNA, with the latter probably corresponding to replicative intermediates produced during viral replication (49, 55).

Since the tagged nsp2 was expressed from an additional

subgenomic RNA (sgRNA) rather than from the genomic RNA as part of pp1a and pp1ab, we analyzed the expression level of the nsp2-GFP fusion protein. To this end, LR7 cells were infected with either MHV-nsp2GFP or MHV-WT at an MOI of 10 and labeled for 3 h with ³⁵S-labeled methionine, starting at 6 h p.i. Cell lysates were processed for immunoprecipitation, followed by SDS-PAGE analysis. The results are shown in Fig. 2F. Antibodies directed against the nsp2 protein precipitated proteins with the expected molecular masses (endogenous mature nsp2, 65 kDa; nsp2-GFP fusion protein, 95 kDa). In addition, a protein with an intermediated molecular mass (71 kDa) was detected, which, like the nsp2-GFP fusion protein, could also be precipitated with antibodies against the GFP tag. The nature of this protein species is unknown, but it was also observed when the nsp2-GFP protein was expressed from a plasmid (data not shown). The radioactivity precipitated was quantified by using PhosphorImager scanning and corrected for the amount of methionines present in the proteins. The results demonstrate that the nsp2-GFP fusion protein was approximately 10-fold more abundant than the endogenous mature nsp2.

Next, we analyzed whether overexpression of the tagged nsp2 affected its localization to the RTCs throughout the infection. To this end, we performed a time-lapse experiment in which MHV-nsp2GFP-infected cells were fixed at different time points p.i. and subsequently processed for immunofluorescence analysis. In this experiment, antibodies directed against nsp4 were used to identify the RTCs (49). The results are shown in Fig. 2D and E. Expression of nsp4, present in distinct foci, could be detected from 4 h p.i. onwards. The maximum level of nsp4 staining was observed at 7 h p.i. Expression of nsp2-GFP could be detected from 5 h p.i., after which the expression level increased until 8 h p.i. Although the cytoplasmic GFP fluorescence at this late time point was higher than at the earlier time points, possibly indicating a saturation of RTCs with nsp2-GFP, the majority of nsp2-GFP was still present in distinct cytoplasmic foci which colocalize with nsp4 (Fig. 2E). In summary, nsp2-GFP or nsp2-mCherry fusion proteins expressed from recombinant MHVs localized to the RTCs, as demonstrated by their colocalization with dsRNA, nsp8, and nsp4 throughout the infection (at least from the time point these fusion proteins become detectable). Importantly, this localization corresponds with the previously reported distribution of nsp2 (5, 21, 24, 62).

nsp2-GFP localizes to DMVs and CMs. To confirm the targeting of nsp2-GFP to the DMV-anchored RTCs, we performed electron microscopy (EM) on infected cells to localize

FIG. 2. Characterization of recombinant MHV-nsp2GFP and subcellular localization of nsp2GFP. (A and B) LR7 cells were infected with MHV-nsp2GFP or MHV-WT (MOI of 10). (A) Culture medium was collected at different time points p.i., after which the viral infectivity was determined by a quantal assay on LR7 cells. The TCID₅₀ values are indicated. (B) Intracellular viral RNA (vRNA) levels were determined by a quantitative RT-PCR on the 1b and the N genes. The data are presented as relative vRNA levels. (C) LR7 cells infected with recombinant MHV-nsp2GFP were fixed and processed for immunofluorescence analysis using antibodies directed against nsp8 and dsRNA. (D and E) LR7 cells infected with recombinant MHV-nsp2GFP were fixed at the indicated time points and processed for immunofluorescence analysis using antibodies directed against nsp4. Images taken from the cells at the different time points were obtained at identical settings (D) while the settings were adjusted to demonstrate the colocalization between nsp2GFP and nsp4 at the 8-h time point (E). (F) Mock-, MHV-WT-, or MHV-nsp2GFP-infected cells were radiolabeled from 6 till 9 h p.i. Cells were lysed and processed for immunoprecipitation with antibodies directed against the nsp2 protein and analyzed by 12.5% SDS-PAGE. The filled triangle indicates the nsp2-GFP protein, the open triangle indicates the endogenous mature nsp2 protein, and the asterisk indicates an additional unidentified protein species.

the protein at the ultrastructural level. First, conventional EM was used to demonstrate the appearance of the DMVs. Their morphology and dimensions (approximately 160 nm in diameter) nicely resembled the structures described previously (23, 61, 65, 72) (Fig. 3A, indicated by the arrowheads). The DMVs often appeared clustered together in the perinuclear region of the cell (data not shown). In between these DMV clusters, reticular inclusions, probably corresponding to the recently described CMs (35), were also observed (Fig. 3A, indicated by the asterisk).

Subsequently, immuno-EM was performed on ultrathin cryo-preparations of MHV-nsp2GFP-infected cells with immunogold labeling specifically directed against the GFP tag. Although the general cellular architecture was preserved, DMVs appeared as empty vesicles in the cryo-sections compared to the ones observed by conventional EM. This dissimilarity is likely due to differences in the fixation methods (35, 65). Mock-infected cells revealed no labeling and no DMVs (data not shown), whereas in MHV-nsp2GFP-infected cells the specific immunogold labeling of nsp2-GFP was observed on both clustered and individual DMVs (Fig. 3B and C, respectively). In addition, nsp2-GFP also decorated CMs (Fig. 3B, asterisk) in between the DMV clusters. These results demonstrate that the nsp2-GFP fusion protein localizes to the MHV-induced DMVs and CMs, confirming the immunofluorescence data, which showed the recruitment of the fusion protein to the RTCs.

Localization of nsp2 on the cytosolic face of the DMVs. The nsp2 protein may either be associated to the cytoplasmic side of the DMVs or, alternatively, be incorporated into the virus-induced vesicles, thereby being shielded from the cytoplasm. Discriminating between these two possibilities was of interest by itself and also because the intended FRAP experiments would only make sense when the nsp2 fusion proteins are not being shielded. In order to facilitate our biochemical analyses of the membrane association of nsp2, we generated another recombinant virus (MHV-nsp2RL) expressing nsp2 fused to *Renilla* luciferase (nsp2-RL). MHV-ERLM (12), which expresses the *Renilla* luciferase (RL) per se was used as a control for our experiments.

First, we verified the membrane recruitment of the nsp2 fusion protein in infected cells. To this end, cells infected with either MHV-ERLM or MHV-nsp2RL were homogenized and subsequently subjected to differential ultracentrifugation such that the cellular membranes were pelleted and separated from the cytosolic fraction. The luciferase expression levels in the different fractions were determined as described in the Materials and Methods section (Fig. 4A). As expected, the majority of the RL protein activity ($\sim 90\%$) was present in the cytosolic fraction of MHV-ERLM-infected cells. In contrast, the large majority of the nsp2-RL fusion protein ($\sim 80\%$) was found in the membrane fraction, in agreement with the idea that nsp2 is recruited to DMVs and CMs.

Next, we performed a protease protection assay on the membrane pellets obtained from the MHV-nsp2RL-infected cells to determine whether the fusion protein was present on the cytosolic face of the DMVs/CMs (i.e., sensitive to protease treatment) or in the interior of these vesicles (i.e., not sensitive to protease treatment). As an internal control, prior to infection cells were transfected with a plasmid expressing a firefly luciferase protein carrying a signal peptide and a KDEL re-

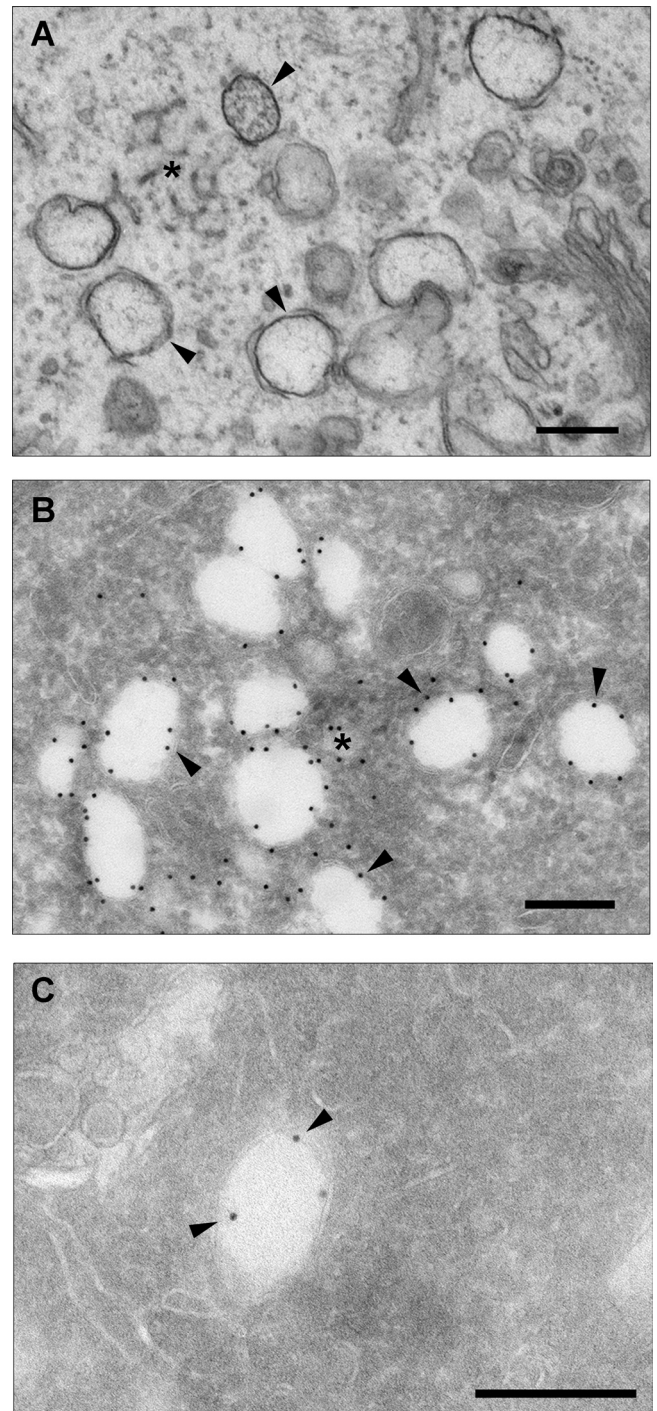


FIG. 3. nsp2-GFP localizes to DMVs and CMs. HeLa-CEACAM1a cells, infected with recombinant MHV-nsp2GFP, were fixed at 8 h p.i. and processed for ultrastructural analysis by chemical fixation and epon embedding (A). Alternatively, cryosections were prepared that were incubated with antibodies directed against the GFP tag, followed by immunogold labeling (B and C). Convoluted membranes are indicated by the asterisks. nsp2 labeling is indicated by the arrowheads. Scale bar, 200 nm.

tention signal at its amino and carboxy termini, respectively, which direct the protein to the ER lumen. The membrane pellets were treated with the serine endopeptidase proteinase K, either in the presence or in the absence of 0.05% Triton

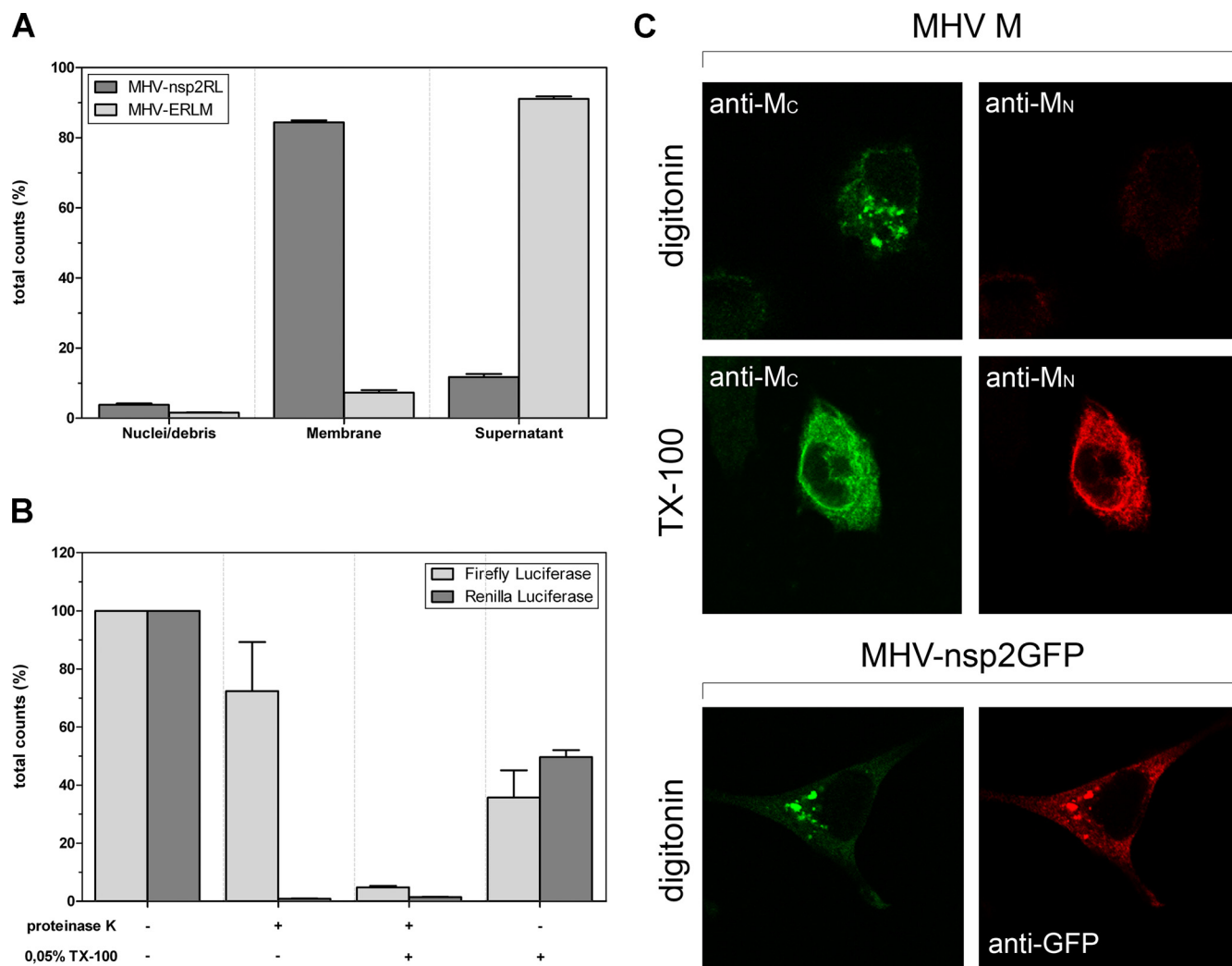


FIG. 4. nsp2 associates to the cytoplasmic face of the DMVs and CMs. (A) LR7 cells infected with MHV-nsp2RL or MHV-ERLM were processed for ultracentrifugation as described in the Materials and Methods section. The luciferase activity in the indicated fractions was determined, corrected for the volume of the fraction, and plotted as the percentage of the total amount of luciferase activity. (B) LR7 cells transfected with pER-Fluc were infected with MHV-nsp2RL. Membrane fractions, prepared as described in the Materials and Methods section, were mock treated with 20 μ g/ml proteinase K in the presence or absence of 0.05% TX-100. *Renilla* and firefly luciferase activities in the differently treated samples were measured and are depicted relative to the mock-treated samples, which are set at 100%. (C) MHV-nsp2GFP-infected LR7 cells were fixed at 6 h p.i. and permeabilized with buffers containing either 0.5 μ g/ml digitonin or 0.1% TX-100. Immunofluorescence was performed using antibodies directed against the N terminus (anti-M_N) or the C terminus (anti-M_C) of the MHV M protein or against the GFP tag (anti-GFP).

X-100, before the protein expression levels of both the firefly and *Renilla* luciferase were assessed. The luciferase levels in the various samples are depicted in Fig. 4B relative to the mock-treated samples. As expected, the ER-localized firefly luciferase protein present in the membrane pellet was almost completely resistant to the proteinase K treatment in the absence, but not in the presence, of Triton X-100, consistent with its localization in the ER lumen. In contrast, regardless of the absence or presence of detergent, nsp2-RL was very sensitive to proteinase K and degraded almost completely. Overall, these results demonstrate that at least the large majority of the nsp2-RL protein is exposed at the exterior of the DMVs/CMs.

To further confirm the localization of nsp2 on the cytoplasmic face of the DMVs/CMs by a different approach, cells were

infected with MHV-nsp2GFP and subsequently subjected to selective permeabilization of the plasma membrane using digitonin before the availability of the GFP tag to specific antibodies was assayed. Triton X-100 was used as a control to permeabilize all cellular membranes. The assay was validated with the MHV membrane (M) protein, the amino and carboxy termini of which are known to reside in the lumen of the secretory pathway and in the cytoplasm, respectively (i.e., N terminus in lumen/C terminus in cytoplasm [N_{exo}/C_{endo}] topology) (53). As shown in Fig. 4C, the MHV M protein could be detected with antibodies directed against its N terminus (anti-M_N) after permeabilization of all cellular membranes with Triton X-100 but not after the selective dissolution of the plasma membrane with digitonin. In contrast, antibodies di-

rected against the carboxy-terminal part of the M protein (anti-M_C) were able to bind the protein after permeabilization with both Triton X-100 and digitonin. As these observations were in perfect agreement with the known topology of the type III M protein, the approach was subsequently applied to cells infected with MHV-nsp2GFP. As shown in Fig. 4C, antibodies directed against the GFP tag were able to readily recognize the fusion protein after permeabilization of cells with digitonin, which is in agreement with the results of the protease protection assay, confirming that the nsp2 protein is exposed on the cytoplasmic face of the DMVs and CMs.

Trafficking of replicative structures. Having established that the nsp2 fusion proteins are recruited to the DMV-anchored RTCs and are suitable for live-cell imaging studies and FRAP analyses, we investigated the real-time dynamics of the nsp2-positive structures. To this end, cells were infected with recombinant MHV expressing either nsp2-GFP or nsp2-mCherry, after which time-lapse recordings were generated over a period of 2 to 2.5 min, with image acquisition every 200 to 300 ms. First, we explored whether the nsp2-positive structures were static or able to move through the cell.

Live-cell imaging of cells infected with MHV-nsp2GFP essentially revealed the presence of two classes of nsp2-GFP-positive structures. One class consisted of relatively large, immobile fluorescent foci (indicated by arrowheads in Fig. 5A). Their only movement appeared to correlate with movements of the cell(s) itself. The other class consisted of small cytoplasmic fluorescent foci, a considerable fraction of which demonstrated a relatively high mobility. In view of the ultrastructural data, we think that the small and large fluorescent foci likely correspond to single DMVs and clusters of DMVs and CMs, respectively.

Two types of movement could be observed for the small fluorescent structures: nsp2-positive foci either (i) demonstrated confined movement (42.3% out of 200 foci tracked) or (ii) moved in a stop-and-go fashion on what appeared to be specific cellular tracks (saltatory movement, 15.0%). The movements of several of the small nsp2-GFP-positive foci were tracked, as indicated by the white lines in Fig. 5A. The complete recording of this movie is shown in Video S1 in the supplemental material. The nsp2-GFP-positive structures numbered 5, 7, and 12 in Fig. 5A displayed confined movements while the others are examples of structures that exhibited saltatory movements. The mean velocity of these latter movements was calculated at $1.3 \pm 0.7 \mu\text{m/s}$, with a peak velocity of $4.1 \mu\text{m/s}$. Occasionally, fluorescent puncta were observed that traveled particularly large distances, clearly revealing the saltatory movement. An example is shown in Fig. 5B (track 1) and in Video S2 in the supplemental material. The peak velocity of this specific displacement was $3.7 \mu\text{m/s}$, with a mean velocity of $1.7 \mu\text{m/s}$.

The characteristics of the movements of the small nsp2-GFP-positive foci (velocity and cellular tracks taken) are suggestive of microtubule-dependent transport (40). Therefore, we investigated whether these structures were associated to microtubules in infected cells. Staining for α -tubulin (Fig. 6A) suggested that the small nsp2-positive foci were associated with or in close proximity to the microtubules. Given the extensive network of microtubules present in the cells, we next performed live-cell imaging experiments to confirm that the mo-

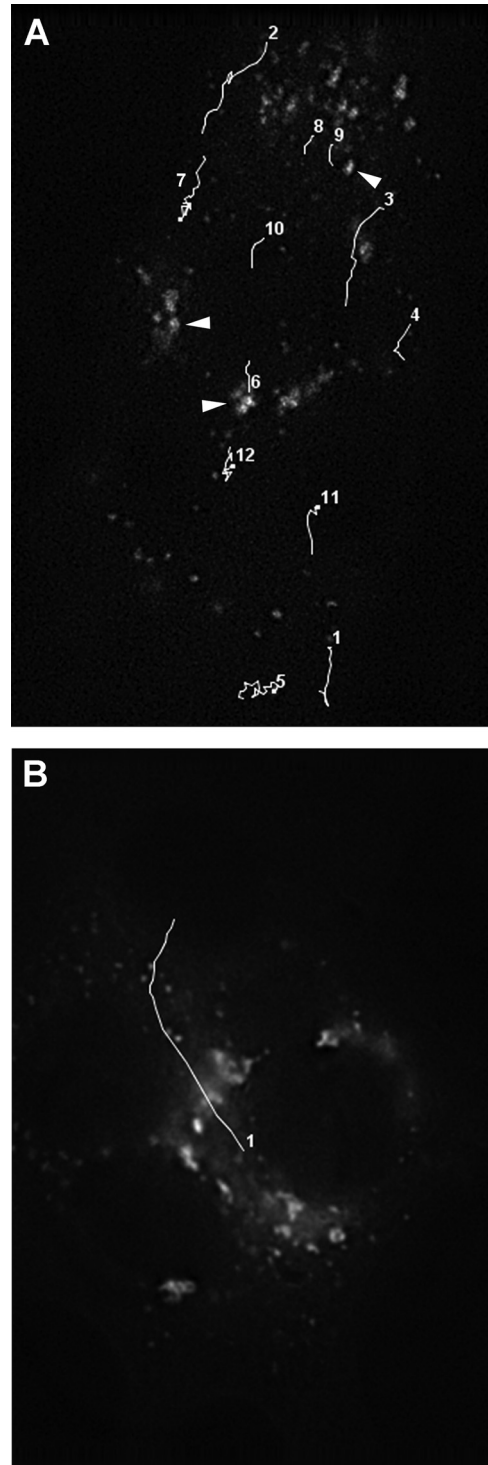


FIG. 5. Trafficking of MHV replicative structures. Time-lapse recordings of MHV-nsp2GFP-infected LR7 cells were obtained using DeltaVision Core (API). Trafficking of selected nsp2-positive structures was determined. Tracks are indicated by white lines and numbered. (A) Tracks 1 to 4, 6, and 8 to 10 represent saltatory movements while tracks 5, 7, and 12 represent confined movements of small nsp2-GFP-positive structures. Track 11 represents confined movement followed by saltatory trafficking. Large, immobile nsp2-positive structures are indicated by the arrowheads. (B) The very long track taken by a small RTC demonstrating saltatory movement is shown. See also Videos S1 and S2 in the supplemental material.

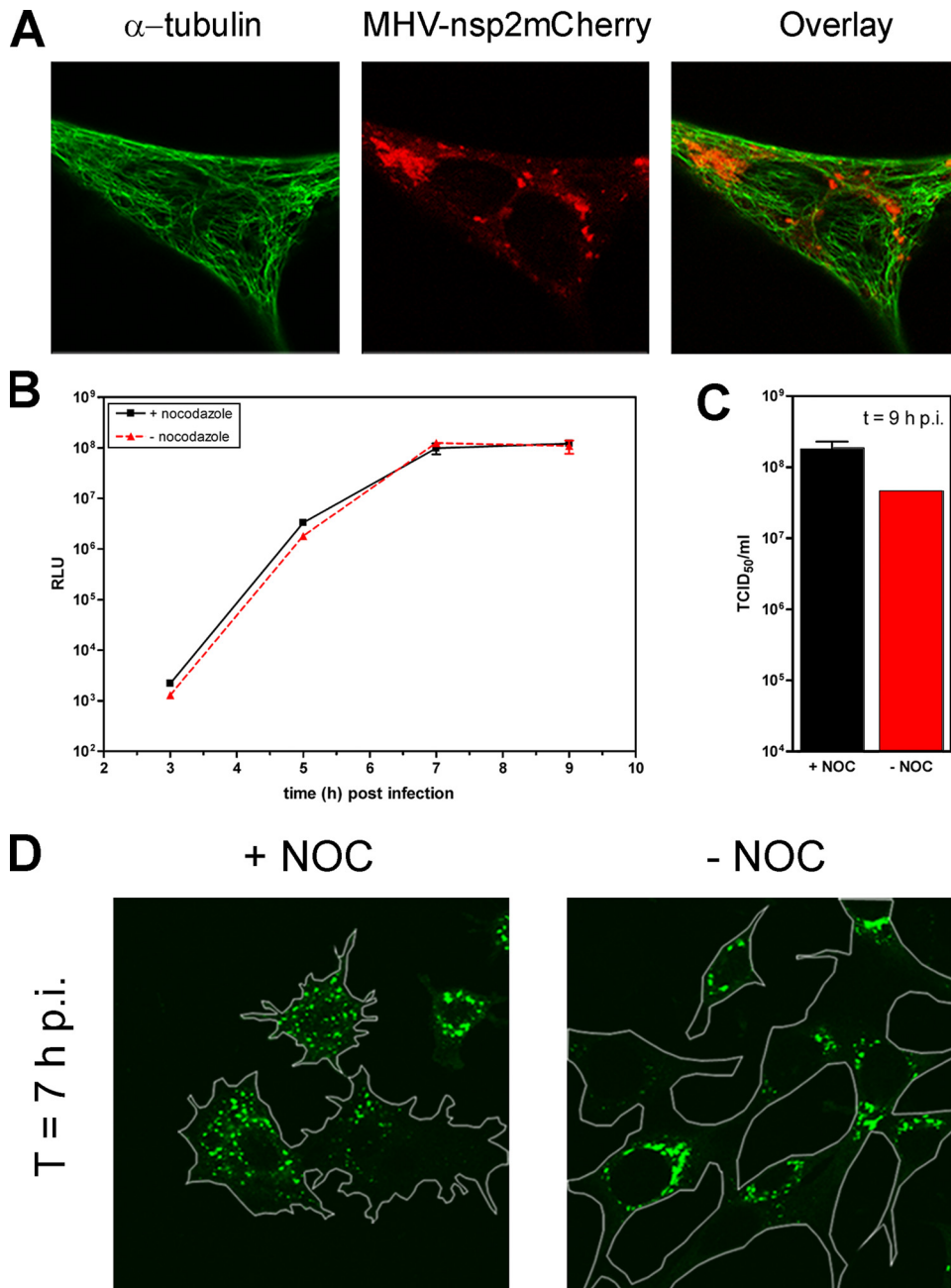
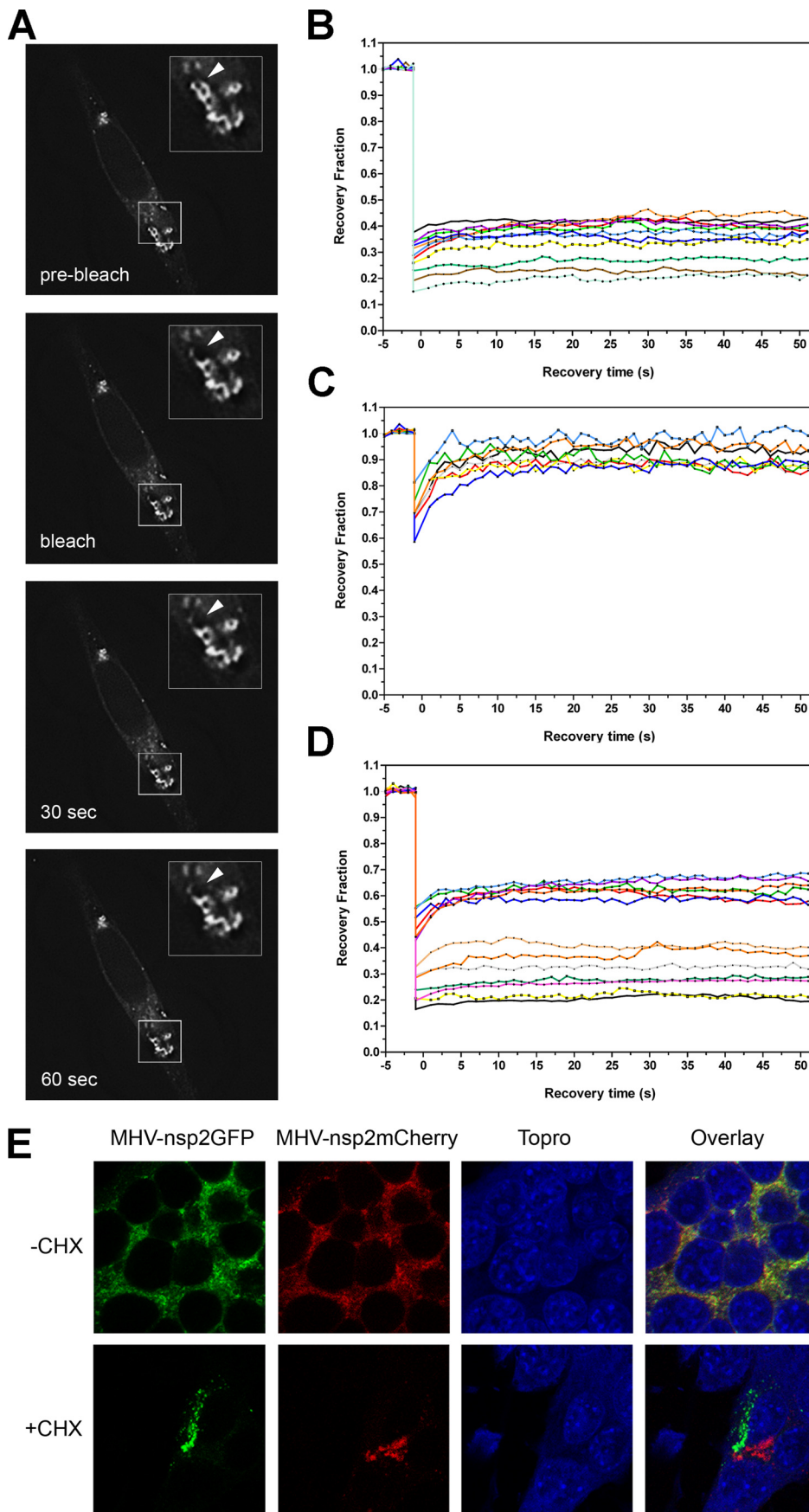


FIG. 6. The role of microtubules in transport. (A) Cells infected with MHV-nsp2mCherry were fixed at 6 h p.i. and processed for immunofluorescence analysis using the α -tubulin antibody to visualize microtubules. (B to D) LR7 cells were infected with MHV-nsp2RL or MHV-nsp2GFP either in the presence (+NOC) or absence (-NOC) of 1 μ M nocodazole. Cells were lysed or fixed at the indicated time point, followed by determination of the luciferase expression levels (B); the TCID₅₀ value of the culture medium was determined (C), or cells were processed for microscopical analysis (D). The white lines in panel D indicate the contours of the cell. T, time.

bility of these small structures was indeed dependent on microtubules. In MHV-nsp2mCherry-infected cells, microtubules were visualized by prior transfection with the plasmid expressing a YFP-alpha-tubulin fusion protein, followed by live-cell imaging. As can be seen in Video S3 in the supplemental material, the small fluorescent foci were in close proximity to the microtubules and appeared to move along these cellular tracks. Furthermore, live-cell imaging was performed in the absence of a functional microtubular network. To this end,

cells were treated with 1 μ M nocodazole, a drug that interferes with the polymerization of microtubules. Treatment of cells with this drug resulted in a complete disruption of the microtubules (data not shown). Importantly, no movement of the fluorescent puncta could be observed under these conditions, as demonstrated in Video S4 in the supplemental material.

Next, we studied whether breakdown of the microtubules affected MHV RNA replication and production of infectious virus particles. To this end, cells treated with nocodazole or



mock treated were infected with a luciferase-expressing recombinant MHV. At different time points p.i., luciferase expression, which is directly correlated to RNA replication (15), and virus production were measured. The nocodazole was kept present throughout the experiment. As shown in Fig. 6B, luciferase expression was not affected by the disruption of microtubules by nocodazole. Moreover, nocodazole treatment also did not affect virus production (Fig. 6C). In agreement with these results, RTCs were still formed in the presence of nocodazole, as demonstrated by the appearance of nsp2-GFP-positive foci at 7 h p.i. (Fig. 6D). However, while in the mock-treated cells the RTCs appeared to be concentrated in the perinuclear region of the cell, in the nocodazole-treated cells, the nsp2-positive foci were scattered throughout the cells. In summary, the results show that the small, but not the large, fluorescent foci were able to move through the cell in a microtubule-dependent fashion. This movement was not, however, essential for MHV RNA replication and the production of infectious virus.

Replicative structures are static entities. Essentially, nothing is known about the dynamics of the coronavirus nsps present at the DMV-anchored RTCs. The RTCs might be relatively static entities, which allow little exchange of proteins with other RTCs, even when these RTCs are anchored to the same DMV; the nsps might be able to move around on a DMV; or the RTCs might even display a continuous exchange of proteins with their cellular environment. We took advantage of our recombinant viruses expressing the fluorescent nsp2 fusion proteins to investigate the dynamics of the replicative structures by means of FRAP analysis. This technique allows measuring the recovery rates of proteins in specific regions of interest (ROI), after irreversible photobleaching, by non-bleached counterparts (reviewed in reference 37). With this assay we are able to determine whether nsp2 recruited to the RTCs is exchanged with nsp2 located outside of the ROI, in the cytoplasm, or at other DMVs. In our experimental set up, ROI were photobleached for 1 s, followed by signal acquisition every second during a period of 60 s. The FRAP assay was first performed on cells infected with MHV-nsp2GFP. Representative images of such an experiment are shown in Fig. 7A. The corresponding fluorescence recovery graphs are depicted in Fig. 7B to D. Photobleached nsp2-GFP-positive structures ($n = 11$) in infected cells (Fig. 7B) demonstrated a reduction of about 60 to 80% of the prebleached fluorescent signal. Essentially no recovery of the fluorescent signal in the ROI was observed over time. Identical results were obtained when only part of a larger fluorescent structure was bleached (data not shown).

As a control, cells were transfected with a plasmid encoding the nsp2-GFP fusion protein and subsequently infected with MHV A59 or mock infected. Next, FRAP experiments were

performed as described above. In the absence of an infection, the nsp2-GFP protein revealed a diffuse cytoplasmic localization, which is in agreement with previous observations (Fig. 1). The photobleached ROI ($n = 8$) in these cells demonstrated a fast recovery of fluorescence within 10 s (Fig. 7C). Moreover, we were unable to bleach the fluorescent signal below $\sim 75\%$ intensity of the prebleach intensity, probably because of the high mobility of the cytoplasmic nsp2-GFP. In contrast, upon infection of the transfected cells with MHV, nsp2-GFP localized to distinct fluorescent foci in the perinuclear region of the cell. When these fluorescent foci were photobleached, no recovery of fluorescence in the ROI ($n = 13$) was observed (Fig. 7D). Apparently, nsp2, once recruited to the RTCs, is not exchanged with nsp2 present in the cytoplasm or in other DMVs.

To verify the lack of exchangeability of nsp2 once recruited to the RTCs, another experiment was performed in which we studied the exchange of fluorescence between preexisting RTCs after fusion of cells expressing either a green or a red fluorescent nsp2. To this end, two LR7 cell cultures were infected, one with MHV-nsp2GFP and the other with MHV-nsp2mCherry, both in the presence of a heptad repeat 2 (HR2) fusion-inhibitory peptide (4). The HR2 peptide was removed at 6 h p.i., after which cells were trypsinized, mixed, and subsequently plated in the presence or absence of cycloheximide (CHX), an inhibitor of protein synthesis. The HR2 peptide was omitted from these cultures to enable cell-cell fusion. The cells were then fixed and processed for microscopy at 9 h p.i. Both in the presence and in the absence of CHX, the formation of syncytia could be observed, as was obvious by the appearance of multinucleated cells. In the absence of CHX, many multinucleated cells were observed that exhibited both green (nsp2-GFP) and red (nsp2-mCherry) fluorescent foci (Fig. 7E, top row). The large majority of these nsp2-GFP- and nsp2-mCherry-positive fluorescent foci were found to colocalize. In contrast, in the presence of CHX, when viral protein synthesis and formation of new RTCs was inhibited (49, 56, 70), no colocalization between nsp2-GFP- and nsp2-mCherry-positive structures was observed in multinucleated cells that were positive for both fusion proteins (Fig. 7E, bottom row). Apparently, while newly synthesized RTCs are able to recruit both fusion proteins, already existing RTCs are not able to exchange or to recruit fluorescent nsp2 fusion proteins. These results are consistent with the lack of fluorescence recovery after photobleaching of nsp2-positive structures and demonstrate that once formed, the replicative structures are static entities.

DISCUSSION

In this study, the dynamics of the coronavirus replicative structures was analyzed for the first time by performing live-

FIG. 7. Coronavirus RTCs are static entities. (A) FRAP was performed on MHV-nsp2GFP-infected cells at 7 h p.i. using the quantifiable laser module of the DeltaVision Core (API). A representative FRAP experiment is depicted, with the bleached area indicated by the white arrowheads in the magnification in the top right corners. (B to D) Fluorescence recovery graphs were generated of bleached ROI either in MHV-nsp2GFP-infected cells (B) or in cells transfected with nsp2-GFP which were subsequently mock infected with MHV-A59 (C) or infected with MHV-A59 (D). (E) Two LR7 cell cultures were infected with either MHV-nsp2GFP or MHV-nsp2mCherry, followed by incubation in the presence of HR2 peptide. At 6 h p.i., the HR2 peptide was removed; cells were trypsinized, mixed, and subsequently plated in the presence (+) or absence (–) of CHX. At 9 h p.i. the cells were processed for immunofluorescence analysis. Nuclear staining was obtained by TOPRO 3 iodide.

cell imaging of coronavirus-infected cells in combination with FRAP analyses. Ideally, one may prefer to visualize these structures by using recombinant viruses expressing tagged versions of an nsp in the context of the replicase precursor proteins; however, such recombinants are currently not available. Therefore, we applied an alternative approach in which the replicative structures were visualized by the expression of fluorescently marked nsp2 proteins in *trans* in MHV-infected cells. Although this protein is dispensable in virus replication and the formation of the viral RTCs (24), this protein was more efficiently recruited to the RTCs than other nsps, at least when expressed in *trans* (data not shown). The tagged nsp2 proteins were found by immunofluorescence analyses to colocalize with several RTC markers, such as nsp8, nsp4, and dsRNA. nsp8 was recently shown to contain RdRp activity and has been proposed to function as a primase (27) while nsp4 has a critical role in directing coronavirus RTC/DMV assembly (9). dsRNA molecules, which are readily detected in coronavirus-infected cells (49), are likely to represent replicative intermediates. Consistently, nsp2-GFP was shown by immuno-EM analysis to be efficiently recruited to the virus-induced DMVs and CMs in MHV-nsp2GFP-infected cells. Previously, newly synthesized viral RNA as well as (viral) dsRNA had been found to be associated with the DMVs (23, 35, 65) while all nsps studied to date have been localized to the DMVs and CMs (16, 24, 49, 51, 61). Taking all these observations together, we conclude that the expressed nsp2 fusion proteins are recruited to the coronavirus RTCs, which are anchored to DMVs. Importantly, this localization corresponds with the previously reported distribution of nsp2 (5, 21, 24, 62).

The nsp2 fusion proteins were associated with the cytoplasmic face of the DMVs/CMs. After selective permeabilization of the plasma membrane, antibodies directed against the GFP tag were able to detect the nsp2 fusion protein. Furthermore, the large majority of the membrane-associated nsp2 was sensitive to protease treatment in the absence of detergents. Apparently, no appreciable fraction of nsp2 was protected by the membranes, which indicates that this protein is not targeted into the lumen of the DMVs. In agreement with the association of nsp2 to the DMV external surface, nsp2-GFP could also be detected in the sections prepared for immuno-EM, in which the DMVs appeared as empty vesicles that lacked the inner membrane. Recently, van Hemert and coworkers (70) demonstrated that dsRNA, nsp5, and nsp8 present in partially purified severe acute respiratory syndrome (SARS)-CoV RTC preparations were protected by membranes from nuclease or protease treatment. Interestingly, however, this was not the case for the very large nsp3. Thus, it appears that some nsps (e.g., nsp5 and nsp8) are protected by membranes, e.g., by their localization inside the DMVs, while others are not (e.g., nsp2 and nsp3). This raises intriguing questions about the overall structure of the coronavirus RTCs and their association with cellular membranes.

As nsp2-GFP was recruited both to single DMVs and to DMV/CM assemblies but not to any other cytoplasmic structure, we conclude that the small, mobile nsp2-positive structures are likely to correspond to single DMVs while the large immobile nsp2-positive structures probably represent the DMV/CM assemblies. Correlative light-electron microscopy, in which live-cell imaging of fluorescently tagged proteins to-

gether with immunogold labeling of ultrathin cryosections of the same cells is combined (71), will be required to unequivocally prove this point. As our results indicate that single DMVs are mobile but that the DMV/CM assemblies are not, one might speculate that newly formed DMVs are able to freely move around until they are "captured" by the DMV/CM assemblies.

The small nsp2-positive foci, supposedly corresponding to single DMVs, traffic through the cell in a microtubule-dependent fashion. Several lines of evidence support this conclusion. The fluorescent structures appeared to traffic on specific cellular tracks, displaying velocities and saltatory movements typical for microtubule-mediated transport (40), while such movements were not observed in the presence of nocodazole. Furthermore, when cells lacking a microtubular network were infected with MHV, the nsp2-positive structures did not accumulate in the perinuclear region of the cell but, rather, were scattered throughout the cytoplasm. Disruption of microtubule-mediated transport of DMVs, however, had no significant impact on coronavirus RNA replication. Trafficking of viral replication complexes along microtubule tracks has previously also been observed for other plus-strand RNA viruses, e.g., HCV (74), poliovirus (10, 19), and the double-stranded DNA vaccinia virus (57). Strikingly, also for these viruses replication was not affected or only modestly affected by the disruption of microtubules (6, 19, 59).

While the trafficking of viral replication complexes along microtubule tracks has been documented for several viruses, the dynamics of these structures has so far been reported in detail only for HCV (74) and vaccinia virus (59). Live-cell imaging of vaccinia virus RTCs demonstrated that only the small (early), and not the large (late), replication sites displayed microtubule motor-mediated motility (59). In the case of HCV, Wölk and coworkers used replicons harboring a GFP insertion in NS5A. Again, two distinct patterns of NS5A-GFP fluorescence were reported: (i) large structures which showed restricted motility and (ii) small structures which showed fast, saltatory movements over large distances. Interestingly, the NS5A-GFP-positive structures displayed a static internal architecture without detectable exchange of NS5A within or in between these structures, as determined by FRAP analyses. Although the experimental approach of this study differs from ours (i.e., the HCV NS5A is an essential replicase protein and was expressed in the context of the viral polyprotein), the dynamics of the HCV replicative structures show several remarkable similarities with those of MHV.

The large MHV DMV/CM assemblies very likely correspond to the recently reported reticulovesicular network of modified ER membranes that is connected to clusters of interconnected DMVs found in SARS-CoV-infected cells (35). From this perspective, it is not surprising that these large assemblies of interconnected ER and DMVs are not able to traffic on microtubule tracks. Interestingly and similar to our observations, movement in HCV and vaccinia virus was observed for only the small RTC assemblies and not the large ones (59, 74). The fast saltatory movements of the small HCV fluorescent foci were shown to occur independently of ER dynamics (74). Whether this also holds true for MHV remains to be established.

Despite the movement of the small nsp2-positive foci, the coronavirus replicative structures turn out to be inherently

static entities. No recovery of fluorescence was observed when (part of) the nsp2-positive structures were photobleached. Apparently, the nsp2 protein, once recruited to the RTCs, is not exchanged by nsp2 protein occurring in the cytoplasm or at other DMVs. This result was confirmed by the observation that preexisting RTCs did not exchange fluorescence after fusion of cells expressing either a green or a red fluorescent nsp2. Our data thus indicate that recruitment of nsp2 occurs only during RTC assembly. Again, similar results were obtained for the HCV RTCs, which also displayed a lack of fluorescence recovery after photobleaching (74). We hypothesize that during RTC assembly, the coronavirus nsp2 is captured within an elaborate network of protein-protein interactions. Indeed, for the nsp2 of SARS-CoV, a large number of viral protein interaction partners have been identified including nsp2, nsp3, nsp6, nsp8, and nsp11 (50, 73). Other coronavirus nsps also appear to be contained in rigid protein-protein interaction networks (28, 50, 73; also unpublished results).

Our findings have important consequences for our understanding of RTC assembly and functioning. The lack of exchange of nsps present in different RTCs fits well with the model of RTC maturation/aging, as has been proposed for coronaviruses (56). In this model, the RNA synthesizing activity of the RTC changes in time, possibly by proteolytic turnover of the replicase polyprotein. Moreover, were nsps generally contained within static networks, complementation between different (e.g., temperature sensitive) viruses carrying a mutation in one of these nsps would have to occur during the formation of these networks at the time of RTC/DMV assembly and would not be possible once these replicative structures had been assembled.

So far, live-cell imaging of viral infections has been limited mainly to the processes of entry and release of viral particles (25, 42). Trafficking and the dynamics of viral replicative structures have received much less attention and for plus-strand RNA viruses have, so far, essentially been reported only for HCV (74) and MHV (this study). Considering that these viruses belong to different virus families (the *Coronaviridae* and the *Flaviviridae*, respectively), the similarities observed between the two viruses are, at least in our opinion, quite remarkable. One feature is the occurrence of differently sized replicative structures, and we have now shown that the small but not the large ones traffic along microtubule tracks. Another, perhaps even more intriguing, feature is that in both cases structures appear to function as rigid entities. In view of the parallels observed between MHV and HCV, it is tempting to hypothesize that our findings reflect general features of the replication of plus-strand RNA viruses.

ACKNOWLEDGMENTS

We thank Corlinda ten Brink from the Cell Microscopy Center, University Medical Centre Utrecht, for technical support and Matthijs Raaben and Mijke Vogels for stimulating discussions. We thank John Flemming, Susan Baker, and Mark Denison for kindly providing antibodies.

This work was supported by grants from the Netherlands Organization for Scientific Research (NWO-VIDI and NWO-ALW) and the Utrecht University (High Potential) to C. A. M. de Haan and F. R. Reggiori.

The funding source had no role in the study design, data collection, analysis, interpretation, or writing of this article.

REFERENCES

1. **Beaudouin, J., D. Gerlich, N. Daigle, R. Eils, and J. Ellenberg.** 2002. Nuclear envelope breakdown proceeds by microtubule-induced tearing of the lamina. *Cell* **108**:83–96.
2. **Bhardwaj, K., L. Guarino, and C. C. Kao.** 2004. The severe acute respiratory syndrome coronavirus Nsp15 protein is an endoribonuclease that prefers manganese as a cofactor. *J. Virol.* **78**:12218–12224.
3. **Bi, W., J. D. Pinon, S. Hughes, P. J. Bonilla, K. V. Holmes, S. R. Weiss, and J. L. Leibowitz.** 1998. Localization of mouse hepatitis virus open reading frame 1A derived proteins. *J. Neurovirol.* **4**:594–605.
4. **Bosch, B. J., R. van der Zee, C. A. de Haan, and P. J. Rottier.** 2003. The coronavirus spike protein is a class I virus fusion protein: structural and functional characterization of the fusion core complex. *J. Virol.* **77**:8801–8811.
5. **Bost, A. G., E. Prentice, and M. R. Denison.** 2001. Mouse hepatitis virus replicase protein complexes are translocated to sites of M protein accumulation in the ERGIC at late times of infection. *Virology* **285**:21–29.
6. **Bost, A. G., D. Venable, L. Liu, and B. A. Heinz.** 2003. Cytoskeletal requirements for hepatitis C virus (HCV) RNA synthesis in the HCV replicon cell culture system. *J. Virol.* **77**:4401–4408.
7. **Brockway, S. M., C. T. Clay, X. T. Lu, and M. R. Denison.** 2003. Characterization of the expression, intracellular localization, and replication complex association of the putative mouse hepatitis virus RNA-dependent RNA polymerase. *J. Virol.* **77**:10515–10527.
8. **Brockway, S. M., and M. R. Denison.** 2005. Mutagenesis of the murine hepatitis virus nsp1-coding region identifies residues important for protein processing, viral RNA synthesis, and viral replication. *Virology* **340**:209–223.
9. **Clementz, M. A., A. Kanjanahaluethai, T. E. O'Brien, and S. C. Baker.** 2008. Mutation in murine coronavirus replication protein nsp4 alters assembly of double membrane vesicles. *Virology* **375**:118–129.
10. **Cui, Z. Q., Z. P. Zhang, X. E. Zhang, J. K. Wen, Y. F. Zhou, and W. H. Xie.** 2005. Visualizing the dynamic behavior of poliovirus plus-strand RNA in living host cells. *Nucleic Acids Res.* **33**:3245–3252.
11. **Decroly, E., I. Imbert, B. Coutard, M. Bouvet, B. Selisko, K. Alvarez, A. E. Gorbalenya, E. J. Snijder, and B. Canard.** 2008. Coronavirus nonstructural protein 16 is a cap-0 binding enzyme possessing (nucleoside-2'-O)-methyltransferase activity. *J. Virol.* **82**:8071–8084.
12. **de Haan, C. A., B. J. Haijema, D. Boss, F. W. Heuts, and P. J. Rottier.** 2005. Coronaviruses as vectors: stability of foreign gene expression. *J. Virol.* **79**:12742–12751.
13. **de Haan, C. A., P. S. Masters, X. Shen, S. Weiss, and P. J. Rottier.** 2002. The group-specific murine coronavirus genes are not essential, but their deletion, by reverse genetics, is attenuating in the natural host. *Virology* **296**:177–189.
14. **de Haan, C. A., K. Stadler, G. J. Godeke, B. J. Bosch, and P. J. Rottier.** 2004. Cleavage inhibition of the murine coronavirus spike protein by a furin-like enzyme affects cell-cell but not virus-cell fusion. *J. Virol.* **78**:6048–6054.
15. **de Haan, C. A., L. van Genne, J. N. Stoop, H. Volders, and P. J. Rottier.** 2003. Coronaviruses as vectors: position dependence of foreign gene expression. *J. Virol.* **77**:11312–11323.
16. **Deming, D. J., R. L. Graham, M. R. Denison, and R. S. Baric.** 2007. Processing of open reading frame 1a replicase proteins nsp7 to nsp10 in murine hepatitis virus strain A59 replication. *J. Virol.* **81**:10280–10291.
17. **Denison, M. R., P. W. Zoltick, S. A. Hughes, B. Giangreco, A. L. Olson, S. Perlman, J. L. Leibowitz, and S. R. Weiss.** 1992. Intracellular processing of the N-terminal ORF 1a proteins of the coronavirus MHV-A59 requires multiple proteolytic events. *Virology* **189**:274–284.
18. **Eckerle, L. D., X. Lu, S. M. Sperry, L. Choi, and M. R. Denison.** 2007. High fidelity of murine hepatitis virus replication is decreased in nsp14 exoribonuclease mutants. *J. Virol.* **81**:12135–12144.
19. **Egger, D., and K. Bienz.** 2005. Intracellular location and translocation of silent and active poliovirus replication complexes. *J. Gen. Virol.* **86**:707–718.
20. **Egloff, M. P., F. Ferron, V. Campanacci, S. Longhi, C. Rancurel, H. Dutartre, E. J. Snijder, A. E. Gorbalenya, C. Cambillau, and B. Canard.** 2004. The severe acute respiratory syndrome-coronavirus replicative protein nsp9 is a single-stranded RNA-binding subunit unique in the RNA virus world. *Proc. Natl. Acad. Sci. U. S. A.* **101**:3792–3796.
21. **Gadlage, M. J., R. L. Graham, and M. R. Denison.** 2008. Murine coronaviruses encoding nsp2 at different genomic loci have altered replication, protein expression, and localization. *J. Virol.* **82**:11964–11969.
22. **Gorbalenya, A. E., L. Enjuanes, J. Ziebuhr, and E. J. Snijder.** 2006. *Nidovirales*: evolving the largest RNA virus genome. *Virus Res.* **117**:17–37.
23. **Gosert, R., A. Kanjanahaluethai, D. Egger, K. Bienz, and S. C. Baker.** 2002. RNA replication of mouse hepatitis virus takes place at double-membrane vesicles. *J. Virol.* **76**:3697–3708.
24. **Graham, R. L., A. C. Sims, S. M. Brockway, R. S. Baric, and M. R. Denison.** 2005. The nsp2 replicase proteins of murine hepatitis virus and severe acute respiratory syndrome coronavirus are dispensable for viral replication. *J. Virol.* **79**:13399–13411.
25. **Greber, U. F., and M. Way.** 2006. A superhighway to virus infection. *Cell* **124**:741–754.
26. **Harcourt, B. H., D. Jukneliene, A. Kanjanahaluethai, J. Bechill, K. M.**

- Severson, C. M. Smith, P. A. Rota, and S. C. Baker. 2004. Identification of severe acute respiratory syndrome coronavirus replicase products and characterization of papain-like protease activity. *J. Virol.* **78**:13600–13612.
27. Imbert, I., J. C. Guillemot, J. M. Bourhis, C. Bussetta, B. Coutard, M. P. Egloff, F. Ferron, A. E. Gorbalenya, and B. Canard. 2006. A second, non-canonical RNA-dependent RNA polymerase in SARS coronavirus. *EMBO J.* **25**:4933–4942.
 28. Imbert, I., E. J. Snijder, M. Dimitrova, J. C. Guillemot, P. Lecine, and B. Canard. 2008. The SARS-coronavirus PLnc domain of nsp3 as a replication/transcription scaffolding protein. *Virus Res.* **133**:136–148.
 29. Ivanov, K. A., T. Hertzog, M. Rozanov, S. Bayer, V. Thiel, A. E. Gorbalenya, and J. Ziebuhr. 2004. Major genetic marker of nidoviruses encodes a replicative endoribonuclease. *Proc. Natl. Acad. Sci. U. S. A.* **101**:12694–12699.
 30. Ivanov, K. A., V. Thiel, J. C. Dobbe, Y. van der Meer, E. J. Snijder, and J. Ziebuhr. 2004. Multiple enzymatic activities associated with severe acute respiratory syndrome coronavirus helicase. *J. Virol.* **78**:5619–5632.
 31. Joseph, J. S., K. S. Saikatendu, V. Subramanian, B. W. Neuman, A. Broun, M. Griffith, K. Moy, M. K. Yadav, J. Velasquez, M. J. Buchmeier, R. C. Stevens, and P. Kuhn. 2006. Crystal structure of nonstructural protein 10 from the severe acute respiratory syndrome coronavirus reveals a novel fold with two zinc-binding motifs. *J. Virol.* **80**:7894–7901.
 32. Kamitani, W., K. Narayanan, C. Huang, K. Lokugamage, T. Ikegami, N. Ito, H. Kubo, and S. Makino. 2006. Severe acute respiratory syndrome coronavirus nsp1 protein suppresses host gene expression by promoting host mRNA degradation. *Proc. Natl. Acad. Sci. U. S. A.* **103**:12885–12890.
 33. Kang, H., K. Bhardwaj, Y. Li, S. Palaninathan, J. Sacchetti, L. Guarino, J. L. Leibowitz, and C. C. Kao. 2007. Biochemical and genetic analyses of murine hepatitis virus Nsp15 endoribonuclease. *J. Virol.* **81**:13587–13597.
 34. Kanjanahaluethai, A., Z. Chen, D. Jukneliene, and S. C. Baker. 2007. Membrane topology of murine coronavirus replicase nonstructural protein 3. *Virology* **361**:391–401.
 35. Knoops, K., M. Kikkert, S. H. Worm, J. C. Zevenhoven-Dobbe, Y. van der Meer, A. J. Koster, A. M. Mommaas, and E. J. Snijder. 2008. SARS-coronavirus replication is supported by a reticulovesicular network of modified endoplasmic reticulum. *PLoS Biol.* **6**:e226.
 36. Kuo, L., G. J. Godeke, M. J. Raamsman, P. S. Masters, and P. J. Rottier. 2000. Retargeting of coronavirus by substitution of the spike glycoprotein ectodomain: crossing the host cell species barrier. *J. Virol.* **74**:1393–1406.
 37. Lippincott-Schwartz, J., E. Snapp, and A. Kenworthy. 2001. Studying protein dynamics in living cells. *Nat. Rev. Mol. Cell Biol.* **2**:444–456.
 38. Locker, J. K., J. K. Rose, M. C. Horzinek, and P. J. Rottier. 1992. Membrane assembly of the triple-spanning coronavirus M protein. Individual transmembrane domains show preferred orientation. *J. Biol. Chem.* **267**:21911–21918.
 39. Lu, X. T., A. C. Sims, and M. R. Denison. 1998. Mouse hepatitis virus 3C-like protease cleaves a 22-kilodalton protein from the open reading frame 1a polyprotein in virus-infected cells and in vitro. *J. Virol.* **72**:2265–2271.
 40. Ma, S., and R. L. Chisholm. 2002. Cytoplasmic dynein-associated structures move bidirectionally in vivo. *J. Cell Sci.* **115**:1453–1460.
 41. Mackenzie, J. 2005. Wrapping things up about virus RNA replication. *Traffic* **6**:967–977.
 42. Marsh, M., and A. Helenius. 2006. Virus entry: open sesame. *Cell* **124**:729–740.
 43. Matthes, N., J. R. Mesters, B. Coutard, B. Canard, E. J. Snijder, R. Moll, and R. Hilgenfeld. 2006. The non-structural protein Nsp10 of mouse hepatitis virus binds zinc ions and nucleic acids. *FEBS Lett.* **580**:4143–4149.
 44. Miller, S., and J. Krijnse-Locker. 2008. Modification of intracellular membrane structures for virus replication. *Nat. Rev. Microbiol.* **6**:363–374.
 45. Minskaia, E., T. Hertzog, A. E. Gorbalenya, V. Campanacci, C. Cambillau, B. Canard, and J. Ziebuhr. 2006. Discovery of an RNA virus 3'→5' exoribonuclease that is critically involved in coronavirus RNA synthesis. *Proc. Natl. Acad. Sci. U. S. A.* **103**:5108–5113.
 46. Namy, O., S. J. Moran, D. I. Stuart, R. J. Gilbert, and I. Brierley. 2006. A mechanical explanation of RNA pseudoknot function in programmed ribosomal frameshifting. *Nature* **441**:244–247.
 47. Narayanan, K., C. Huang, K. Lokugamage, W. Kamitani, T. Ikegami, C. T. Tseng, and S. Makino. 2008. Severe acute respiratory syndrome coronavirus nsp1 suppresses host gene expression, including that of type I interferon, in infected cells. *J. Virol.* **82**:4471–4479.
 48. Oostra, M., M. C. Hagemeijer, M. van Gent, C. P. Bekker, E. G. te Lintelo, P. J. Rottier, and C. A. de Haan. 2008. Topology and membrane anchoring of the coronavirus replication complex: not all hydrophobic domains of nsp3 and nsp6 are membrane spanning. *J. Virol.* **82**:12392–12405.
 49. Oostra, M., E. G. te Lintelo, M. Deijs, M. H. Verheije, P. J. Rottier, and C. A. de Haan. 2007. Localization and membrane topology of coronavirus nonstructural protein 4: involvement of the early secretory pathway in replication. *J. Virol.* **81**:12323–12336.
 50. Pan, J., X. Peng, Y. Gao, Z. Li, X. Lu, Y. Chen, M. Ishaq, D. Liu, M. L. Dediego, L. Enjuanes, and D. Guo. 2008. Genome-wide analysis of protein-protein interactions and involvement of viral proteins in SARS-CoV replication. *PLoS One* **3**:e3299.
 51. Prentice, E., J. McAuliffe, X. Lu, K. Subbarao, and M. R. Denison. 2004. Identification and characterization of severe acute respiratory syndrome coronavirus replicase proteins. *J. Virol.* **78**:9977–9986.
 52. Raaben, M., A. W. Einerhand, L. J. Taminiau, M. van Houdt, J. Bouma, R. H. Raatgeep, H. A. Buller, C. A. de Haan, and J. W. Rossen. 2007. Cycloxygenase activity is important for efficient replication of mouse hepatitis virus at an early stage of infection. *Virol. J.* **4**:55.
 53. Rottier, P. J., G. W. Welling, S. Welling-Wester, H. G. Niesters, J. A. Lenstra, and B. A. Van der Zeijst. 1986. Predicted membrane topology of the coronavirus protein E1. *Biochemistry* **25**:1335–1339.
 54. Salonen, A., T. Ahola, and L. Kaariainen. 2005. Viral RNA replication in association with cellular membranes. *Curr. Top. Microbiol. Immunol.* **285**:139–173.
 55. Sawicki, S. G., D. L. Sawicki, and S. G. Siddell. 2007. A contemporary view of coronavirus transcription. *J. Virol.* **81**:20–29.
 56. Sawicki, S. G., D. L. Sawicki, D. Younker, Y. Meyer, V. Thiel, H. Stokes, and S. G. Siddell. 2005. Functional and genetic analysis of coronavirus replicase-transcriptase proteins. *PLoS Pathog.* **1**:e39.
 57. Schepis, A., B. Schramm, C. A. de Haan, and J. K. Locker. 2006. Vaccinia virus-induced microtubule-dependent cellular rearrangements. *Traffic* **7**:308–323.
 58. Schonborn, J., J. Oberstrass, E. Breyel, J. Tittgen, J. Schumacher, and N. Lukacs. 1991. Monoclonal antibodies to double-stranded RNA as probes of RNA structure in crude nucleic acid extracts. *Nucleic Acids Res.* **19**:2993–3000.
 59. Schramm, B., C. A. de Haan, J. Young, L. Doglio, S. Schleich, C. Reese, A. V. Popov, W. Steffen, T. Schroer, and J. K. Locker. 2006. Vaccinia-virus-induced cellular contractility facilitates the subcellular localization of the viral replication sites. *Traffic* **7**:1352–1367.
 60. Seybert, A., C. C. Posthuma, L. C. van Dinten, E. J. Snijder, A. E. Gorbalenya, and J. Ziebuhr. 2005. A complex zinc finger controls the enzymatic activities of nidovirus helicases. *J. Virol.* **79**:696–704.
 61. Shi, S. T., J. J. Schiller, A. Kanjanahaluethai, S. C. Baker, J. W. Oh, and M. M. Lai. 1999. Colocalization and membrane association of murine hepatitis virus gene 1 products and De novo-synthesized viral RNA in infected cells. *J. Virol.* **73**:5957–5969.
 62. Sims, A. C., J. Ostermann, and M. R. Denison. 2000. Mouse hepatitis virus replicase proteins associate with two distinct populations of intracellular membranes. *J. Virol.* **74**:5647–5654.
 63. Slot, J. W., and H. J. Geuze. 2007. Cryosectioning and immunolabeling. *Nat. Protoc.* **2**:2480–2491.
 64. Snijder, E. J., P. J. Bredenbeek, J. C. Dobbe, V. Thiel, J. Ziebuhr, L. L. Poon, Y. Guan, M. Rozanov, W. J. Spaan, and A. E. Gorbalenya. 2003. Unique and conserved features of genome and proteome of SARS-coronavirus, an early split-off from the coronavirus group 2 lineage. *J. Mol. Biol.* **331**:991–1004.
 65. Snijder, E. J., Y. van der Meer, J. Zevenhoven-Dobbe, J. J. Onderwater, J. van der Meulen, H. K. Koerten, and A. M. Mommaas. 2006. Ultrastructure and origin of membrane vesicles associated with the severe acute respiratory syndrome coronavirus replication complex. *J. Virol.* **80**:5927–5940.
 66. Sparks, J. S., E. F. Donaldson, X. Lu, R. S. Baric, and M. R. Denison. 2008. A novel mutation in murine hepatitis virus nsp5, the viral 3C-like proteinase, causes temperature-sensitive defects in viral growth and protein processing. *J. Virol.* **82**:5999–6008.
 67. Sutton, G., E. Fry, L. Carter, S. Sainsbury, T. Walter, J. Nettleship, N. Berrow, R. Owens, R. Gilbert, A. Davidson, S. Siddell, L. L. Poon, J. Diprose, D. Alderton, M. Walsh, J. M. Grimes, and D. I. Stuart. 2004. The nsp9 replicase protein of SARS-coronavirus, structure and functional insights. *Structure* **12**:341–353.
 68. Taguchi, F., and J. O. Fleming. 1989. Comparison of six different murine coronavirus JHM variants by monoclonal antibodies against the E2 glycoprotein. *Virology* **169**:233–235.
 69. Thiel, V., K. A. Ivanov, A. Putics, T. Hertzog, B. Schelle, S. Bayer, B. Weissbrich, E. J. Snijder, H. Rabenau, H. W. Doerr, A. E. Gorbalenya, and J. Ziebuhr. 2003. Mechanisms and enzymes involved in SARS coronavirus genome expression. *J. Gen. Virol.* **84**:2305–2315.
 70. van Hemert, M. J., S. H. van den Worm, K. Knoops, A. M. Mommaas, A. E. Gorbalenya, and E. J. Snijder. 2008. SARS-coronavirus replication/transcription complexes are membrane-protected and need a host factor for activity in vitro. *PLoS Pathog.* **4**:e1000054.
 71. van Rijnsoever, C., V. Oorschot, and J. Klumperman. 2008. Correlative light-electron microscopy (CLEM) combining live-cell imaging and immunolabeling of ultrathin cryosections. *Nat. Methods* **5**:973–980.
 72. Verheije, M. H., M. Raaben, M. Mari, E. G. te Lintelo, F. Reggiori, F. J. van Kuppeveld, P. J. Rottier, and C. A. de Haan. 2008. Mouse hepatitis coronavirus RNA replication depends on GBF1-mediated ARF1 activation. *PLoS Pathog.* **4**:e1000088.
 73. von Brunn, A., C. Teepe, J. C. Simpson, R. Pepperkok, C. C. Friedel, R. Zimmer, R. Roberts, R. Baric, and J. Haas. 2007. Analysis of intraviral protein-protein interactions of the SARS coronavirus ORF6ome. *PLoS One* **2**:e459.
 74. Wolk, B., B. Buclehe, D. Moradpour, and C. M. Rice. 2008. A dynamic view of hepatitis C virus replication complexes. *J. Virol.* **82**:10519–10531.

75. **Wurdinger, T., M. H. Verheije, M. Raaben, B. J. Bosch, C. A. de Haan, V. W. van Beusechem, P. J. Rottier, and W. R. Gerritsen.** 2005. Targeting non-human coronaviruses to human cancer cells using a bispecific single-chain antibody. *Gene Ther.* **12**:1394–1404.
76. **Zhai, Y., F. Sun, X. Li, H. Pang, X. Xu, M. Bartlam, and Z. Rao.** 2005. Insights into SARS-CoV transcription and replication from the structure of the nsp7-nsp8 hexadecamer. *Nat. Struct. Mol. Biol.* **12**:980–986.
77. **Ziebuhr, J., E. J. Snijder, and A. E. Gorbalenya.** 2000. Virus-encoded proteinases and proteolytic processing in the *Nidovirales*. *J. Gen. Virol.* **81**:853–879.
78. **Zust, R., L. Cervantes-Barragan, T. Kuri, G. Blakqori, F. Weber, B. Ludewig, and V. Thiel.** 2007. Coronavirus non-structural protein 1 is a major pathogenicity factor: implications for the rational design of coronavirus vaccines. *PLoS Pathog.* **3**:e109.